EES Batteries

ROYAL SOCIETY OF CHEMISTRY

PAPER

View Article Online
View Journal

Check for updates

Cite this: DOI: 10.1039/d6eb00013d

Dry-milled microstructure-controlled sulfide electrolytes enabling superionic transport and high-capacity all-solid-state batteries

Ziyu Lu,[a,b] Siwu Li,[a] Lin Li,[b] Ziling Jiang,[b] Long Chen,*[c] Miao Deng,[b] Chen Liu[d] and Chuang Yu*[a,b,d]

Received 19th January 2026,
Accepted 13th April 2026

DOI: 10.1039/d6eb00013d

rsc.li/EESBatteries

Ball-milled solid-state electrolytes exhibit remarkable room-temperature ionic conductivity exceeding 10 mS cm^{-1}, yet the mechanisms underlying this exceptional performance remain insufficiently understood. In this study, we systematically explore the influence of filling rate of milling balls (FRB) and ball-to-material ratio (BMR) on the structure–property relationships of $Li_{5.5}PS_{4.5}Cl_{0.8}Br_{0.7}$ (LPSCB) argyrodite electrolytes. Optimal conditions were found at 10% FRB and 80 : 1 BMR, yielding a superior ionic conductivity of 13.3 mS cm^{-1} and activation energy of 0.28 eV after sintering. Rietveld refinement reveals that milling parameters do not alter the cubic argyrodite phase ($F\bar{4}3m$), but significantly affect defect density and residual stress. The enhanced performance arises from defect engineering and stress relaxation, rather than lattice expansion, challenging the conventional view that lattice expansion enhances Li^+ diffusion. The optimized electrolyte demonstrates stable performance (13–14 mS cm^{-1}) across different loadings, highlighting its potential for all-solid-state battery applications. Li_2TiS_3 (LTS) cathode material was employed to systematically evaluate the electrochemical performance and failure mechanisms of LTS/LPSCB/Li–In all-solid-state lithium batteries (ASSLBs). Electrochemical testing of batteries shows a reversible capacity of 470.6 mAh g^{-1} and 96.22% capacity retention after 200 cycles under conventional loading (7.6 mg cm^{-2}). Impedance analysis suggests that Li^+ diffusion dominates battery kinetics. Under higher load conditions (14 mg cm^{-2}), stable high-energy output is achieved, though accelerated stress growth over 400 cycles leads to interfacial cracking and capacity decay. These findings validate the feasibility of LTS as a cathode material for high-load ASSLBs, emphasizing that effective stress management at the anode interface is essential for ensuring long-term cycling stability in high-energy-density ASSLBs.

Broader context

All-solid-state lithium batteries (ASSLBs) offer superior safety and energy density over conventional systems. Their commercial viability depends on solid-state electrolytes (SSEs) with high conductivity and interfacial stability. Sulfide-based argyrodites show promise, but how ball-milling parameters influence their structure–property relationship remains unclear. This work goes beyond conventional optimization by linking milling kinetics to the performance of a halogen-rich $Li_{5.5}PS_{4.5}Cl_{0.8}Br_{0.7}$ argyrodite. We demonstrate that ionic transport is governed not by lattice expansion but by defect engineering and residual stress modulation, dictated by ball filling rate and ball-to-material ratio—challenging a common assumption. Using an optimized electrolyte and a Li_2TiS_3 cathode, we construct high-performance ASSLBs and unravel failure mechanisms under conventional and high-mass-loading conditions. Results show that while high energy density is achievable, long-term cycling stability is limited by interfacial stress evolution, especially at the anode. This study provides a refined understanding of synthesis–structure–property correlations in mechanochemically prepared SSEs and offers a practical evaluation pathway for high-loading ASSLBs, highlighting stress management as a critical frontier alongside ionic conductivity for durable, high-energy-density solid-state batteries.

1. Introduction

To address the escalating climate crisis driven by the intensified consumption of fossil fuels, researchers worldwide have increasingly focused on batteries as vital components for enabling renewable energy storage and utilization.[1] Among various battery technologies, power batteries for electric vehicles stand out as a key area of development. Presently,

---

[a] *School of Information Mechanics and Sensing Engineering, Xidian University, Xi'an, Shaanxi 710126, P. R. China. E-mail: cyu_msubmit@163.com*
[b] *School of Chemistry and Chemical Engineering, Huazhong University of Science and Technology, Wuhan 430074, P. R. China*
[c] *Key Laboratory for Ultrafine Materials of Ministry of Education, School of Chemical Engineering, East China University of Science and Technology, 130 Meilong Road, Shanghai, 200237 China. E-mail: longchen@ecust.edu.cn*
[d] *School of Electrical and Electronic Engineering, Huazhong University of Science and Technology, Wuhan, 430074, P. R. China*

nearly all commercially available power batteries are based on liquid electrolytes.[2,3] However, these liquid electrolyte batteries face challenges such as limited energy density and safety concerns during practical operation.[4] As a result, all-solid-state lithium batteries (ASSLBs) have attracted significant attention as promising candidates for next-generation energy storage systems.[5–7] The defining characteristic of ASSLBs is their use of solid-state electrolytes (SEs), which facilitate ionic conduction while effectively blocking electronic conduction. Moreover, the mechanical rigidity of solid electrolytes plays a crucial role in suppressing the growth of lithium dendrites.[8] Over the past decade, extensive research has been conducted on the properties of solid-state electrolytes—including electrochemical window, ionic conductivity, and air stability—giving rise to four mainstream technological pathways: oxides, polymers, halides, and sulfides.[9–11] However, most solid-state electrolytes remain hindered by their substantially lower Li^+ transport rates compared to liquid electrolytes, which fundamentally limits their applicability in fast-charging technologies. Sulfide-based solid-state electrolytes (SEs) are widely considered the most promising electrolyte pathway, owing to their ultrahigh ionic conductivity at room temperature and excellent reduction stability. Nevertheless, before commercial adoption can be achieved, several major challenges must be understood and overcome for SEs.

The primary challenge lies in optimizing the fabrication processes for SEs.[12,13] Current research tends to focus predominantly on the ultimate electrochemical performance metrics of SEs, while systematic exploration of scalable and reproducible preparation methods remains relatively underdeveloped.[14,15] This gap has spurred the emergence of diverse synthesis techniques, including liquid-phase synthesis, solid-state sintering, and mechanochemical ball milling. For instance, Choi *et al.* synthesized bromine- and iodine-doped Li_6PS_5X precursors using acetonitrile (ACN) as the solvent, achieving an ionic conductivity on the order of 10^{-4} S cm^{-1} after subsequent sintering.[16] Overall, the liquid-phase synthesis route offers advantages such as homogeneous product formation and lower processing costs. However, it is often associated with relatively moderate ionic conductivity and potential environmental concerns related to solvent use. Otoyama *et al.* systematically optimized the grinding jar volume and grinding bead mass based on prior research. After grinding for 40–70 hours, they successfully synthesized Li_3PS_4 and Li_4SnS_4 solid-state electrolytes, both of which demonstrated ionic conductivities in the range of 10^{-4} to 10^{-3} S cm^{-1}.[17,18] Separately, Zhuo *et al.* adopted a combined ball-milling and sintering approach. In their procedure, raw materials were weighed in stoichiometric proportions and placed into a 50 mL zirconia milling jar, along with grinding balls of 4 mm and 10 mm diameters. The mixture was milled at 550 rpm for 30 hours, followed by sintering at 300 °C for 12 hours. This process yielded the solid-state electrolyte $Li_{5.3}PS_{4.3}Cl_{0.85}Br_{0.85}$, which exhibited an ionic conductivity as high as 9 mS cm^{-1}.[19] Overall, the combined ball-milling and sintering method offers notable advantages, including a relatively simple process, excellent product properties, and broad applicability in the fabrication of various solid-state electrolytes. Among the various preparation methods, the ball milling process parameters are considered the most critical factor in the synthesis of electrolyte precursors. Existing research has predominantly focused on optimizing parameters such as sintering temperature and time for specific SEs.[20] However, systematic studies have yet to establish clear correlations between ball-milling parameters, the resulting microstructural evolution during sintering, and the final ionic conductivity.[21] Therefore, investigating process routes based on ball milling, with an emphasis on maximizing ion conductivity, is essential for optimizing the design of sulfide electrolytes, improving preparation efficiency, and unlocking their full application potential.

Additionally, poor oxidation stability remains a significant limitation of SEs.[22] The incompatibility between the electrochemical window of sulfide electrolytes and oxide cathodes leads to severe decomposition reactions, which cause interfacial failure and a rapid degradation in battery performance. Current research aimed at improving oxidation stability has made notable advancements, focusing primarily on three key strategies: one approach involves doping and modifying sulfide electrolytes, such as through oxygen or fluorine doping, to broaden their electrochemical window.[23] Another strategy employs a dual-layer electrolyte configuration, which prevents direct contact between the sulfide electrolyte and the active cathode material, thereby effectively mitigating the oxidation-induced decomposition of the SEs.[24] Finally, the oxide coating strategy involves the nanoscale encapsulation of active cathode materials using oxides that exhibit high compatibility with sulfide electrolytes, such as ZrO_2, $LiNbO_3$, and Li_2WO_4.[25] This approach aims to alleviate issues such as strain-induced cracking and decomposition in cathode materials. However, these strategies often come with high costs and complex processing requirements, which pose significant barriers to the practical implementation and widespread adoption of ASSLBs. Therefore, identifying a cathode active material that offers excellent intrinsic compatibility with sulfide electrolytes and can be prepared through a simplified process represents a promising direction for advancing ASSLBs technology. In recent years, the metal sulfide TiS_2 has attracted considerable attention owing to its favorable ion/electron transport properties and electrochemical stability. To further improve energy density, Hu *et al.* investigated a class of lithium-rich layered metal sulfides ($Li_{1+x}M_yS_2$, where M = Fe, Ti, *etc.*).[26] They successfully synthesized the Li_2TiS_3 active material and integrated it into an all-solid-state lithium–indium battery, achieving a maximum discharge capacity of 423.3 mAh g^{-1} at 0.1C (0.33 mA cm^{-2}) with a capacity retention rate of 95%. These results provide valuable insights for developing high-energy all-solid-state batteries based on sulfide electrolytes. Nevertheless, the performance of LTS cathode materials under high-loading conditions remains underexplored, and further studies are required to systematically evaluate their electrochemical behavior and mechanical properties.

Building on the insights outlined above, this study aims to achieve ultra-high ionic conductivity by optimizing the ball-milling process for the preparation of LPSCB SEs. The objective is to establish a universal optimization strategy for the fabrication of ball-milled SEs. Focusing on the ionic transport properties of the electrolyte, key preparation parameters, such as the optimal FRB and BMR, were systematically determined. By combining scanning electron microscopy (SEM) and X-ray diffraction (XRD) techniques with Rietveld refinement, the study examined the mechanisms by which ball milling parameters influence microstructural properties, including electrolyte surface morphology, particle size, and unit cell dimensions. In parallel, the consistency of ionic conductivity under high electrolyte loading was systematically characterized. Subsequently, Li_2TiS_3 was employed as the cathode active material to fabricate ASSLBs, and its electrochemical performance was evaluated. Through *in situ* electrochemical impedance spectroscopy, *in situ* pressure monitoring, and a suite of microscopic analyses, the physicochemical evolution within the high-loading ASSLBs was comprehensively investigated. These findings offer practical guidance for realizing high-energy sulfide-based ASSLBs *via* compatibility-oriented design at the electrode level.

2. Experimental section

2.1. Sample synthesis

The raw materials used to synthesize the LPSCB solid-state electrolyte were Li_2S (Aladdin, ≥99.8%), P_2S_5 (Macklin, ≥99%), LiCl (Aladdin, ≥99%), and LiBr (Macklin, ≥99.9%). Li_2S, P_2S_5, LiCl, and LiBr were weighed based on the reaction stoichiometry equation and ball-milled for 16 h at 500 rpm using WC balls in a planetary mill. Fig. S1 (shown in SI) displays the XRD patterns of the electrolyte at different milling times; the peaks of the raw materials gradually weakened as the milling time increased, and the impurity peaks completely disappeared when the milling time reached 16 hours. The produced powders were then sintered in a muffle furnace for 6 hours at 500 °C, with the temperature rising at a rate of 2 °C min^{-1}.[20,27] The Li_2TiS_3 used as a cathode electrode is synthesized from Li_2S (Aladdin, ≥99.8%) and TiS_2 (Aladdin, ≥99.5%). The precursors were weighed in stoichiometric proportions, placed into a WC milling jar, and high-energy ball milled at 500 rpm for 30 h. All synthesis steps were performed under an argon atmosphere (H_2O and O_2 levels < 0.01 ppm).

2.2. Materials characterization

Solid electrolyte powders were ground with an agate mortar and sieved through a 300-mesh stainless-steel sieve inside an argon-filled glovebox (H_2O and O_2 levels < 0.01 ppm). The sieved powder was subsequently stored in airtight vials under an argon atmosphere until further use.

X-ray diffraction (XRD) patterns were recorded on a Rigaku SmartLab-SE diffractometer equipped with a Cu Kα radiation source. Measurements were performed over a 2θ range of 10°–80° at a scan rate of 5.0° min^{-1}. Raman spectroscopy was conducted under protected conditions to avoid air exposure. Approximately 5 mg of sample was loaded into borosilicate quartz capillaries (1.5 mm outer diameter) and sealed with rubber stoppers inside the glovebox. Raman spectra were acquired using a LabRAM HR800 spectrometer with a 532 nm laser excitation source. For scanning electron microscopy (SEM), a small amount of powder was lightly adhered to conductive carbon tape inside the glovebox. The sample was then transferred under vacuum to a TESCAN MIRA LMS microscope and imaged in secondary-electron mode at an accelerating voltage of 5 kV and a working distance of 3 mm. Particle size analysis was performed on the obtained SEM images using Nanomeasure software.

2.3. Electrochemical measurements

The entire battery fabrication process was performed in an argon-filled glovebox. The synthesized electrolyte powder or cathode material was pressed into thin pellets (100 mg each) at 450 MPa using a mold. Ionic conductivity of the pellets was measured with an electrochemical workstation (Squidstat Plus, Admiral) over a frequency range of 2 MHz to 0.1 Hz under an AC amplitude of 50 mV. DC polarization tests were carried out with the same pressing method and equipment, wherein the electronic conductivity was determined by applying constant voltages of 0.5 V, 1 V, and 1.5 V for 1800 s at each voltage. Since the cathode material exhibits both ionic and electronic conductivity, an electron-blocking symmetric cell with an LPSCB/LTS/LPSCB configuration was fabricated to evaluate the ionic conductivity. For the assembly, 50 mg of LPSCB electrolyte was placed on each side, while 100 mg of LTS powder constituted the middle layer. The cell was pressed under the same conditions as previously described. To isolate the contribution of the LTS layer, the impedance of the full cell was corrected by subtracting the impedance of 100 mg of LPSCB electrolyte. The ionic conductivity of the LTS layer was then determined based on its measured thickness.

For battery performance evaluation, composite cathodes were prepared by mixing Li_2TiS_3, the target electrolyte, and VGCF at a mass ratio of 60 : 35 : 5. The mixture was milled in a ZrO_2 grinding jar at 300 rpm for 2 h. In all-solid-state batteries, the conventional composite cathode loading was 6 mg (7.6 mg cm^{-2}), while a higher loading of 11 mg (14 mg cm^{-2}) was also adopted. A solid electrolyte pellet (100 mg) was first compacted at 450 MPa by layer pressing. The composite cathode powder was then uniformly applied on one side, and a Li–In alloy foil was attached on the opposite side as the anode. Charge–discharge performance, cycling stability, and related metrics were evaluated using a NEWARE CT-400 battery tester within specified voltage windows and at various current rates. For *in situ* impedance analysis, EIS spectra of cells with high cathode loading were acquired at intervals during charge–discharge cycling between 0.9 and 2.4 V. The cycling protocol consisted of 20 cycles each at 0.1C and 0.5C rates. Subsequent relaxation time analysis was conducted using the distribution of relaxation times (DRT) toolbox in MATLAB. For *in situ* pressure measurements, a full cell (with identical structure and component loadings) was assembled in a custom mold equipped with high-precision pressure sensors. Pressure variations during cycling were recorded at a frequency of once per minute. All experiments were carried out at room temperature.

3. Results and discussion

In the preparation of solid-state electrolyte powders, several key parameters influence the high-energy ball milling process. Among these, ball mill speed and grinding time are commonly used to control electrolyte impurity content and crystallinity, making them the focus of extensive research. However, the FRB and the BMR are often determined empirically, lacking a solid theoretical foundation. Fig. 1a illustrates the experimental setup used to investigate the impact of milling parameters. A 10 mm diameter milling bead and stoichiometric LPSCB electrolyte raw materials were placed in a 50 mL ball milling jar. Three variations of FRB and BMR were tested (FRB: 5%, 10%, and 20%; BMR: 20 : 1, 40 : 1, and 80 : 1), resulting in a series of ball milling samples.

Scanning electron microscopy (SEM) revealed the surface morphology of the ball-milled electrolyte (Fig. 1b–f). The ball-milled electrolyte displayed an irregular mixture of powder and bulk phases. The 5% FRB sample contained a significantly higher proportion of larger electrolyte bulk particles compared to the 10% FRB and 20% FRB samples. This finding was supported by particle size analysis, which showed that the 5% FRB electrolyte had an average particle size of approximately 20 micrometers, while the 10% and 20% FRB samples had average particle sizes of around 3 micrometers (Fig. S2, shown in SI). The milling energy provided by 5% FRB appeared insufficient to achieve uniform fragmentation of the electrolyte particles. In terms of ball-to-material ratios, the electrolyte morphology showed minimal differences between the 20 : 1 and 40 : 1 BMR ratios, with both exhibiting partial particle agglomeration. In contrast, the 80 : 1 BMR electrolyte exhibited a more uniform particle distribution.

Fig. 1g compares the ionic conductivity and activation energy of electrolytes milled with three different ball-filling

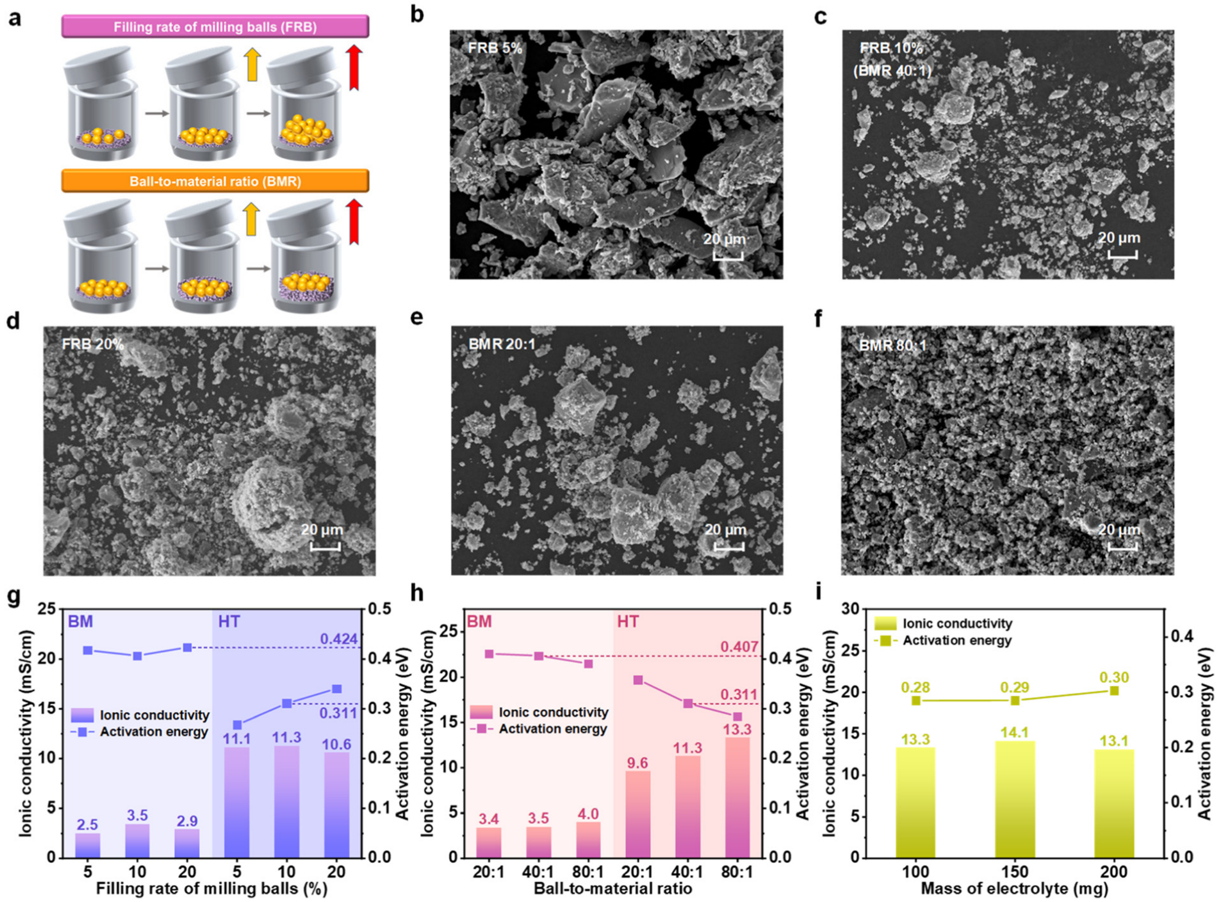

Fig. 1 (a) Schematic diagram of key technical parameters for the ball milling process. scanning electron microscope (SEM) images of SEs synthesized at filling rates of milling balls of (b) 5%, (c) 10% and (d) 20% and ball-to-material ratios of (e) 20 : 1 and (f) 80 : 1. Comparison of ionic conductivity and activation energy of LPSCB SEs synthesized with different (g) filling rates of milling balls and (h) ball-to-material ratios. (i) Ionic conductivity and activation energy of LPSCB SEs at three mass loads.

ratios. When the FRB was increased to 10%, the ionic conductivity of the milled electrolyte peaked at 3.5 mS cm^{-1}, before subsequently decreasing. After sintering at 500 °C, the ionic conductivity of all three samples increased to over 10 mS cm^{-1}, with the 10% FRB sample maintaining the highest conductivity. Interestingly, the trends in activation energy before and after sintering were inconsistent across the three samples. The activation energy of the ball-milled electrolyte alone varied by only 0.02 eV, showing minimal dependence on FRB content. Following sintering, the SE activation energy for the 5% FRB sample decreased to 0.27 eV, while that for the 20% FRB sample was 27.2% higher than the 5% FRB value. This observation contradicts the conclusion that the 10% FRB sample provides the optimal electrolyte ion transport capability, highlighting a non-monotonic relationship between conductivity (σ) and activation energy (E_a). For the unsintered electrolyte, the 5% FRB sample provides insufficient energy, resulting in fewer particle collisions and minimal defect formation in the crystals, which leads to a coarse powder. Since Li-ion transport in the cold-pressed pellet before sintering is governed primarily by porosity, the room-temperature conductivity remains low. During sintering, the 5% FRB sample experiences minimal abnormal grain growth, resulting in fine grains with numerous random, high-angle grain boundaries. These boundaries are characterized by disordered atomic structures and low local migration barriers, leading to the lowest activation energy. Overall, the difference in room-temperature ionic conductivity between the 5% FRB and 10% FRB samples is relatively small, with both FRB values falling within a reasonable range. However, in practical milling processes, the mass of grinding balls is typically several orders of magnitude greater than that of the raw materials. To optimize grinding efficiency, selecting a 10% FRB value for the milling parameters is considered the most effective approach. Building on this, electrolytes were prepared using three different ball-to-powder ratios, and their ionic conductivity and activation energy were subsequently measured (Fig. 1h). Increasing the ball-to-material ratio was found to enhance the ionic conductivity of the electrolyte while simultaneously reducing its activation energy. This trend remained consistent across both pre- and post-sintered samples. These results suggest that variations in the ball-to-powder ratio primarily influence the collision probability between the milling balls and the powder, rather than the total mechanical energy imparted per unit mass of powder. Given sufficient milling time, the mechanical energy tends to accumulate to a comparable saturation level. Consequently, the internal defect state and particle-size distribution of the electrolyte powders converge before sintering. During sintering, all three samples follow similar densification and grain-boundary evolution pathways, resulting in virtually identical grain-boundary characteristics and final microstructures. As a result, no desynchronization between σ and E_a is observed. At the same ball milling time, a higher ball-to-material ratio enhances the ion transport capability of the electrolyte. When the mass ratio of balls to material reaches 80 : 1, the LPSCB electrolyte achieves the highest ionic conductivity (13.3 mS cm^{-1}) and the lowest activation energy (0.28 eV). To further validate the ion transport capability of the optimized electrolyte following ball milling, the ionic conductivity and activation energy of the thicknesses of the 100 mg, 150 mg, and 200 mg electrolyte sheets were measured and shown in Fig. 1i. The ionic conductivity of LPSCB electrolytes remained stable between 13–14 mS cm^{-1} across all three loading levels, with activation energies ranging from 0.28 to 0.30 eV. These findings confirm the stable and reliable performance of LPSCB electrolytes under these conditions, demonstrating their potential for practical applications.

Under varying milling ball filling rates and ball-to-material ratios, the composite electrolytes consistently form a percolating ceramic network that exhibits ultrahigh room-temperature ionic conductivity exceeding 10 mS cm^{-1}. However, such exceptional ion transport capability cannot be solely attributed to the formation of a three-dimensional ceramic scaffold; additional contributions from impurity phases or lattice distortions may also play a significant role.[28] Fig. 2a presents the X-ray diffraction (XRD) patterns of LPSCB electrolytes prepared under three distinct FRB conditions. The main diffraction peaks of all samples correspond to the stibnite crystal structure. For the 5% FRB milling condition, a residual Li_2S precursor peak is observed in the as-milled powder, indicating that 5% FRB is insufficient to achieve a homogeneous LPSCB precursor. This peak disappears after sintering, with no new secondary phases emerging, suggesting that the residual Li_2S either dissolves into the lattice or volatilizes during heat treatment. The resulting loss of S^{2-} may introduce deep-level defects, which could explain the non-monotonic relationship between σ and E_a observed for this electrolyte.[29] While such defects do not immediately obstruct ionic conduction pathways, they may serve as latent triggers for interfacial side reactions or internal short-circuits under elevated voltages or prolonged cycling. LiCl diffraction peaks were detected in all sintered electrolytes, a secondary phase commonly observed in LPSCB-type conductors. This phenomenon arises because the larger ionic radius of Br^- compared to Cl^- increases the formation energy of the 4d site. To maintain local charge balance, the lattice preferentially expels Cl^- as LiCl, which then precipitates at grain boundaries.[30] Existing studies suggest that such a minor LiCl fraction does not significantly impair ionic transport.[27] The X-ray diffraction (XRD) patterns of the electrolyte prepared under different ball-to-material ratios (BMR) are shown in Fig. 2b. At low ball-to-powder weight ratios, Li_2S impurity peaks remain visible after milling, indicating that the precipitation of this phase is closely linked to whether the total mechanical energy input is sufficient. Notably, no LiCl diffraction peaks are detected in the sintered sample prepared with a high ball-to-powder ratio of 80 : 1, which can be attributed to the higher collision frequency and energy density at this ratio, which facilitate the amorphization of LiCl.

To elucidate the underlying mechanisms by which ball-milling parameters affect the ion transport properties of the electrolyte, it is essential to go beyond a qualitative discussion

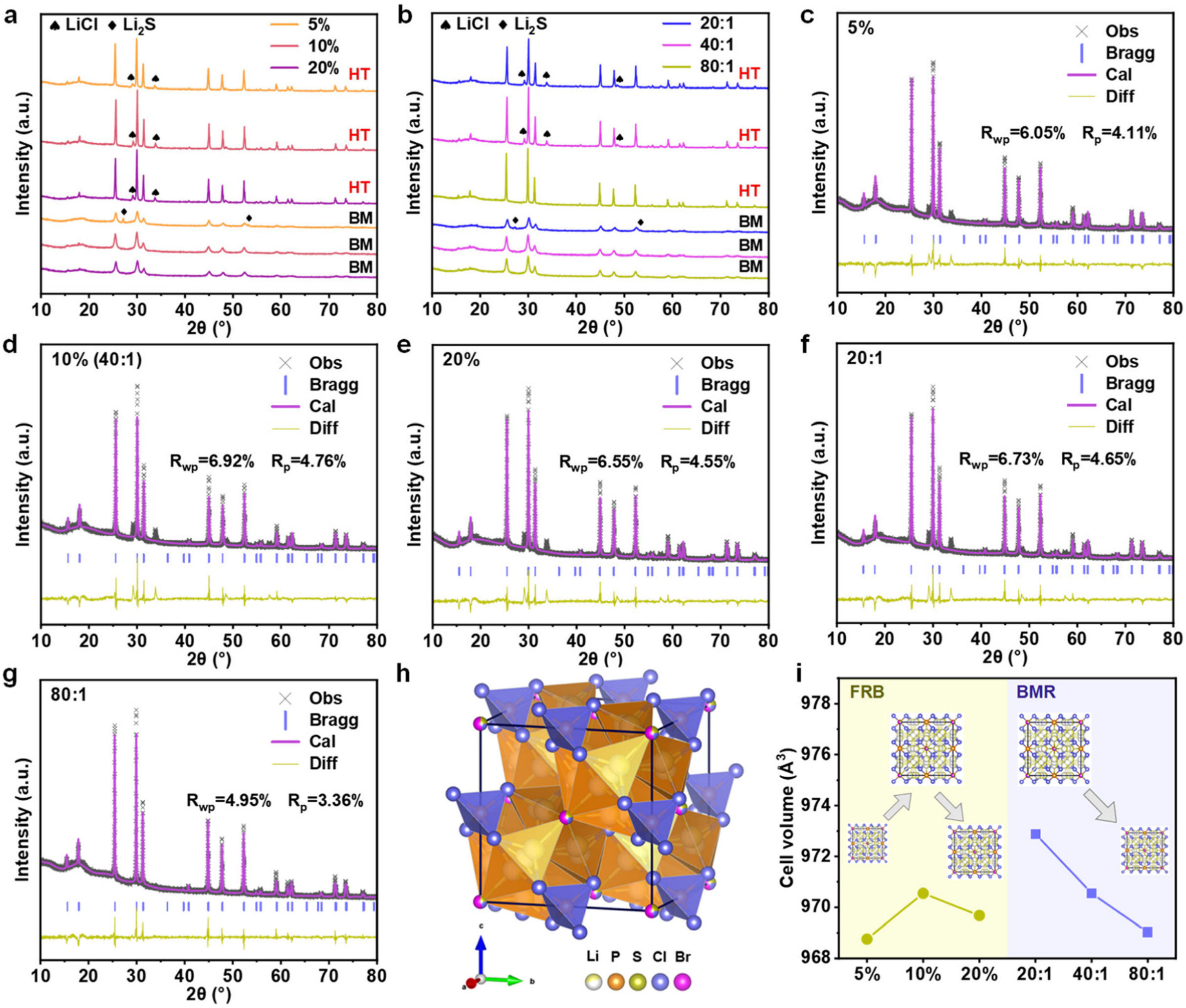

Fig. 2 XRD patterns of LPSCB electrolyte before and after sintering under different ball-milling conditions: (a) filling rate of milling balls and (b) ball-to-material ratios. (c) Crystal structure of LPSCB electrolyte after optimized ball milling process. Rietveld refinements of SEs synthesized under conditions of filling rate of milling balls of (d) 5%, (e) 10%, and (f) 20%, and ball-to-material ratios of (g) 20 : 1 and (h) 80 : 1. (i) Evolution of the electrolyte's unit-cell parameters with ball-milling conditions.

of impurity phases and conduct a quantitative analysis of the evolution of the electrolyte's intrinsic crystal structure. To this end, we performed Rietveld refinement on the X-ray diffraction (XRD) patterns of all electrolyte samples (specific refinement parameters are shown in Tables S1–S5 in the SI). The refined diffraction patterns are presented in Fig. 2c–g. Building on established literature, the parameters of the selected crystal structural model were iteratively optimized. The corresponding refined diffraction patterns are shown in Fig. 2c–g. The resultant R_{wp} and R_p values for all specimens meet the expected criteria, thereby validating the structural model employed. This finding also confirms that alterations in the ball-milling parameters, specifically the FRB and BMR, do not induce discernible phase transformations within the electrolyte crystal lattice. A schematic representation of the cubic argyrodite-phase crystal structure for the LPSCB electrolyte, derived from the refinement results, is provided in Fig. 2h. The structure belongs to the cubic argyrodite phase (space group $F\bar{4}3m$). In this framework, PS_4^{3-} and S^{2-} ions collectively form a rigid anionic lattice, which serves as the lithium-ion conduction pathway.[31] Halide ions, such as Cl^-/Br^-, occupy some of the 4a and 4d sites in a disordered manner, functioning as a "chemical valve" that modulates both charge transport and the dimensions of the conduction channels.

Fig. 2i presents the evolution of unit cell parameters derived from Rietveld refinement. As the FRB increases, the unit cell volume of the LPSCB electrolyte first increases and then decreases, reaching a maximum at 10% FRB. The expansion and contraction of the unit cell volume closely mirror the trend observed in electrolyte ionic conductivity, with a larger unit cell volume correlating to higher ionic conductivity. However, under varying ball-to-material ratios, the unit cell volume consistently decreases as the ball-to-material ratio increases, which is accompanied by an increase in ionic conductivity. This behavior contradicts findings from previous studies, which generally postulate that an increase in unit cell volume leads to a larger lithium-ion diffusion bottleneck, thereby enhancing ionic conductivity and reducing activation energy.[32] Consequently, it can be inferred that lattice spacing alone does not govern the intrinsic Li^+ transport rate within the crystal. Rather, the modulation of ionic conductivity by ball-milling parameters is primarily driven by the interplay of energy input, defect density, and residual stress.

In the FRB parameter, the only variable is the collision-site density: an increase in the number of milling balls enhances the collision frequency experienced by the powder per unit time. When FRB is increased from 5% to 10%, the additional mechanical energy results in a higher concentration of intrinsic vacancies and dislocations. These defects not only expand the lattice parameter but also provide additional mobile charge carriers, thereby improving conductivity. However, when FRB is further increased to 20%, the excess energy promotes defect coalescence and triggers abnormal grain growth, which enhances the grain-boundary blocking effect and partially suppresses fast ionic transport. For the BMR, the key physical change involves the collision energy density imparted per unit mass of powder and the relative contributions of shear and impact stresses. At a low BMR of 20 : 1, the powder bed is thick, and individual particles are primarily consolidated through repeated "squeeze–friction" actions, limiting the shear component. As BMR increases to 80 : 1, the powder mass decreases significantly, and particles are more readily trapped between opposing ball layers, subjecting them to multiple reciprocating shear events. Consequently, a higher BMR amplifies the shear-impact fraction, which in turn increases the residual stress, local temperature spikes, and the degree of amorphization within the powder. The experimentally observed monotonic decrease in unit-cell volume with increasing BMR, alongside the positive correlation between BMR and ionic conductivity, can be explained as follows. The 80 : 1 BMR powder accumulates a larger amount of elastic and plastic strain energy before sintering; during heating, this energy is released first, resulting in effective stress relaxation through defect elimination and lattice rearrangement.[33,34] As a result, the lattice contracts to a near-equilibrium dimension, yielding the smallest refined cell parameter. In contrast, the 20 : 1 BMR powder receives insufficient mechanical energy and experiences a lower degree of plastic deformation; furthermore, the elastic potential energy stored in it lacks sufficient thermodynamic driving force, and its residual stresses are not fully dissipated before sintering.[35] As a result, a portion of tensile strain remains in the lattice, leading to an apparently "inflated" unit-cell volume.

Addressing the oxidative stability limitation of sulfide-based electrolytes is essential for fully exploiting the electrochemical potential of the superionic conductor LPSCB. Li_2TiS_3, exhibiting excellent chemical compatibility with sulfide electrolytes, was therefore synthesized and employed in the assembly of ASSLBs.[36] XRD and Raman spectroscopy were employed to verify the physical structure of the synthesized LTS, and its electrochemical performance was subsequently assessed (Fig. S3 and S4, shown in SI). Results confirm that the synthesized LTS demonstrates exceptional ion and electron transport capabilities. Using conventional fabrication procedures, an LTS/LPSCB/Li–In battery was constructed with a composite cathode loading of 7.6 mg cm^{-2}. Fig. 3a presents the rate performance of the ASSLBs. Discharge capacities of 483.1, 412.7, and 263.6 mAh g^{-1} were achieved at discharge rates of 0.1C, 0.5C, and 1C, respectively, indicating stable rate performance at rates below 1C, with notable capacity loss at higher discharge rates. Upon reversing the C-rate, a reversible capacity of 451.2 mAh g^{-1} was attained at 0.2C, demonstrating exceptional reversible cycling capability. Analysis of the charge–discharge curves at varying rates reveals a decrease in coulombic efficiency with increasing discharge rate, suggesting a significant rise in internal polarization, which likely exacerbates irreversible side reactions or promotes additional charge loss pathways (Fig. S5, shown in SI). Charge–discharge measurements were subsequently performed over multiple cycles within a voltage window of 0.9–2.4 V (*vs.* Li–In) at a rate of 0.5C under ambient conditions (Fig. 3b). Unlike previously reported ASSLBs employing NCM-type or lithium cobalt oxide cathodes, which typically deliver coulombic efficiencies (CE) below 100%, the LTS-based battery exhibited an initial discharge capacity of 380.6 mAh g^{-1} with a first-cycle CE of 112%. After ten cycles, the anomalously high CE decreased to 100.3% and remained nearly constant at approximately 100.0% up to the 100th cycle. Concurrently, both charge and discharge capacities increased, reaching 470.1 mAh g^{-1} and 470.3 mAh g^{-1}, respectively. Such evolution indicates that continuous yet reversible Li^+ insertion into the LTS cathode occurred during cycling. Formation of various sulfide species, originating from minor surface oxidation of LTS during synthesis, is considered primarily responsible for this charge-compensation behavior.[37] Activation and subsequent diffusion of S_n^{2-} ions induced by excess Li^+ insertion further contribute to the gradual capacity enhancement observed over extended cycling.[26] Furthermore, the voltage hysteresis observed in the ASSLB warrants attention. The initial polarization voltage of the LTS/LPSCB/Li–In battery was approximately 0.09 V, increasing only slightly to 0.10 V after 100 cycles. Such minimal voltage growth confirms the high stability of Li^+ transport in the LTS cathode against the LPSCB electrolyte and suggests effective suppression of severe oxidative decomposition of the sulfide electrolyte, a common issue arising from interfacial problems at the cathode. Fig. 3c presents the cycling performance of the LTS/LPSCB/Li–In battery at 0.5C. Over the first 60 cycles, the battery's capacity steadily increased, reaching a peak discharge capacity of 470.6 mAh g^{-1} at the 62nd charge–discharge cycle. After 200 cycles, the capacity retention rate remained high at 96.22% (*vs.* 470.6 mAh g^{-1}), further demonstrating the battery's exceptional cycling stability. Additionally, the EIS spectra of the battery before and after cycling were compared (Fig. 3d). Notably, the overall impedance of the ASSLB decreased significantly after cycling compared to its pre-cycling state, indicating that the Li^+ transport pathways within the battery were opti-

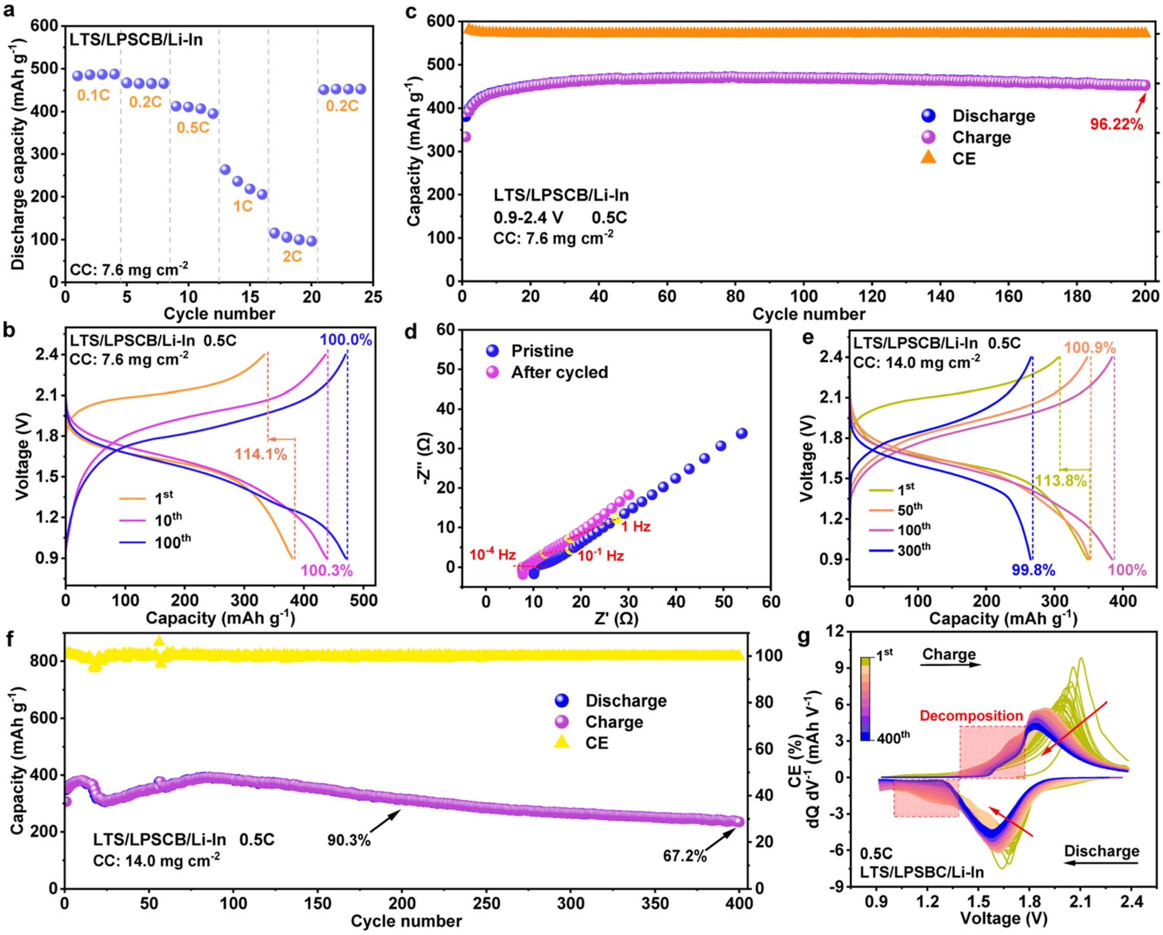

Fig. 3 Electrochemical performance of LTS/LPSCB/Li–In ASSLBs. (a) Rate performance, (b) Charge–discharge curves, and (c) cycling performance of ASSLBs at 0.5C under conventional composite cathode loading. (d) EIS spectra of ASSLBs before and after long-term cycling. (e) Charge–discharge curves, (f) long-cycle performance, and (g) d*Q*/d*V* curves of LTS/LPSCB/Li–In ASSLBs at high composite cathode loading.

mized through the charge–discharge process. It is hypothesized that the initial interface between LTS and the electrolyte may have exhibited localized weak physical contacts, which were gradually consolidated under the influence of electrochemical stress, thereby enhancing the overall activation of LTS. Furthermore, a noticeable shift in the positions of the real and imaginary parts at the same frequency in the impedance spectrum was observed, which will be discussed in further detail later.

Investigation of the electrochemical behavior of LTS cathodes under high loading conditions was conducted by increasing the composite cathode loading to 14 mg cm^{-2}. Fig. 3e presents the charge–discharge curves of the high-loading LTS/LPSCB/Li–In battery at 0.5C. The first-cycle discharge capacity reached 384.4 mAh g^{-1} with a coulombic efficiency (CE) of 113.8%. Consistent with previous observations, the discharge capacity gradually increased over several initial cycles before exhibiting a gradual decline in subsequent cycles. The CE stabilized near 100% and decreased slowly thereafter, implying that the LTS cathode maintained full charge capacity release during the early cycling phase even under high loading conditions. A pronounced reduction in the voltage plateau was observed by the 300th cycle, while the CE decreased to 99.8%, reflecting the progressive accumulation of irreversible capacity loss within the battery. Long-term cycling tests further revealed pronounced capacity fluctuations in the LTS/LPSCB/Li–In batteries (Fig. 3f). After 200 cycles, the discharge capacity remained at 314.5 mAh g^{-1}, corresponding to a capacity retention of 90.3% relative to 348.4 mAh g^{-1}. By 400 cycles, the retention decreased substantially to 67.2%. These findings demonstrate that the LTS/LPSCB/Li–In battery can deliver high energy density even under elevated cathode loading, albeit at the cost of shortened cycle life. Notably, two distinct capacity increase phases emerged within the first 100 cycles, suggesting a complex interplay of mechanisms between the LTS cathode and the LPSCB electrolyte. Possible contributing factors include capacity compensation from transient polysulfide species, partial capacity contribution from oxidative decomposition of the LPSCB electrolyte, and continuous capacity fading associated with hindered Li$^+$ transport across the solid–solid interfaces.[38–40]

Elucidation of the redox behavior in the cathode region of high-loading ASSLBs during cycling was achieved through analysis of the corresponding differential capacity (dQ/dV) curves (Fig. 3g). The delithiation and lithiation processes of the LTS cathode are reflected by a dominant oxidation peak between 1.8–2.4 V in the charge profile and a primary reduction peak between 1.4–1.8 V in the discharge profile, respectively. With increasing cycle number, both peaks gradually shift toward lower potentials, accompanied by a reduction in peak intensity —behavior consistent with the dual degradation mechanism widely reported in ASSLBs, involving the depletion of active material and the consumption of active lithium.[41] Progressive accumulation of ohmic polarization and over-lithiated products during repeated cycling induces irreversible structural deterioration of LTS, transforming it from an ordered, lithium-rich configuration into a disordered, lithium-deficient state.[42] Such an irreversible transformation directly accounts for the continuous capacity decay of the battery. Notably, a broad hump appears in the reduction profile within the 1.0–1.4 V region during the initial 200 cycles, gradually weakening and ultimately disappearing in later cycles. The emergence of this feature correlates with the coulombic efficiency exceeding 100% and likely originates from the irreversible reduction of short-chain sulfides and Ti^{2+} species produced by over-lithiation of LTS. With extended cycling, the number of electrochemically active sites on the sulfur framework progressively declines, while the increasing thickness of interfacial byproducts further impedes ionic contact between the bulk LTS and the solid electrolyte. Such interfacial blockage suppresses reactivity and ultimately eliminates the reduction hump. During the oxidation process, a shoulder peak emerges in the 1.4–1.8 V range, which can be attributed to the delithiation of these side products.

All-solid-state lithium batteries (ASSLBs) display distinctive electrochemical characteristics across different potential regions. A detailed depiction of this kinetic behavior was achieved by constructing the charge–discharge profile of the LTS/LPSCB/Li–In battery as a function of time under high composite cathode loading (Fig. 4a). Key potentials along the profile were selected as sampling points for electrochemical impedance spectroscopy (EIS), collectively representing various states of charge (SOC) throughout the charge–discharge process. *In situ* EIS spectra obtained for the pristine and 20-cycled LTS/LPSCB/Li–In battery at 0.1C are presented in Fig. 4b. Conventional ASSLBs generally exhibit one or more distinct semicircles in the high-frequency region, followed by a 45° sloping line at low frequency. In sharp contrast, the EIS response of the LTS/LPSCB/Li–In system is characterized by a faint arc combined with a dominant sloping line, implying that diffusion processes govern the overall electrochemical behavior. Low interfacial and bulk resistances further confirm the highly efficient Li^+ transport enabled by the superior ionic conductivity of the LPSCB electrolyte. Evolution of impedance during charge–discharge cycling reveals consistent patterns both before and after extended operation. As the battery charges from 0.9 V to 1.9 V, overall resistance decreases with increasing potential, followed by a gradual rise within the 1.9–2.4 V range. During discharge, impedance declines progressively down to 1.6 V and subsequently increases below this potential. Such voltage-dependent impedance variation highlights the presence of multiple electrochemical stages governing the redox dynamics within the LTS/LPSCB/Li–In battery.

Clarification of the mechanisms underlying the observed variations was achieved through the distribution of relaxation times (DRT) analysis applied to the *in situ* EIS data. Corresponding DRT spectra were derived and visualized as two-dimensional intensity plots (Fig. S6 and Fig. 4c, shown in SI). Analysis of the DRT curves at 0.1C reveals that the major impedance peaks are concentrated within the time-constant region where τ exceeds 0.1 s. Based on the peak distribution, the time domain can be divided into three characteristic regions. Region T1 encompasses contributions from bulk electrolyte resistance, grain boundary effects, and interfacial impedance between the electrolyte and both electrodes. Region T2 corresponds to charge-transfer processes occurring within the electrode, whereas region T3 predominantly represents diffusion-related phenomena, including electrode reactions and the transport of reaction products.[43] In the pre-cycling DRT spectra, impedance peaks within the T2 and T3 regions shift toward shorter τ values during charging and revert to longer τ values during discharge. A shift of the low-frequency peak toward smaller relaxation times signifies accelerated ionic diffusion kinetics, while the reverse shift toward higher τ indicates kinetic retardation induced by obstruction of effective diffusion pathways. Such a reversible, bidirectional evolution directly illustrates the dynamic coupling between lithium-ion diffusion and progressive interfacial blockage by side-reaction products.[44,45] After repeated charge–discharge cycles, the low-frequency peak in the later charging stage exhibits a pronounced shift toward higher frequencies, accompanied by a significant enhancement in peak intensity within the T3 region. Such spectral evolution indicates irreversible interfacial degradation. Accumulation of over-lithiated products increases diffusion resistance, whereas the observed peak displacement primarily reflects a polarization-induced nonequilibrium kinetic effect. Impedance evolution of the LTS/LPSCB/Li–In battery throughout cycling can be rationalized by four distinct kinetic stages. In the initial charging phase between 0.9 V and 1.9 V (activation stage), stress relaxation following deep lithiation and re-oxidation of surface side products dominates the process, giving rise to a decline in impedance. As the potential continues to increase during the LTS delithiation stage, progressive Li^+ depletion within the lattice constrains ion transport pathways, resulting in a pronounced impedance rise caused by accumulated polarization. During subsequent discharge, voltage reduction from 2.4 V to 1.6 V corresponds to the LTS lithiation stage, where restored Li^+ concentration facilitates ionic transport and reduces impedance. A final stage emerges during deep discharge below 1.6 V, characterized by the formation of sulfide and Ti^{2+} species that progressively obstruct diffusion pathways, leading to a renewed impedance increase. Additionally, *in situ* impedance measurements were conducted on ASSLBs cycled at 0.5C (Fig. S7, shown in SI). Although high current density obscures

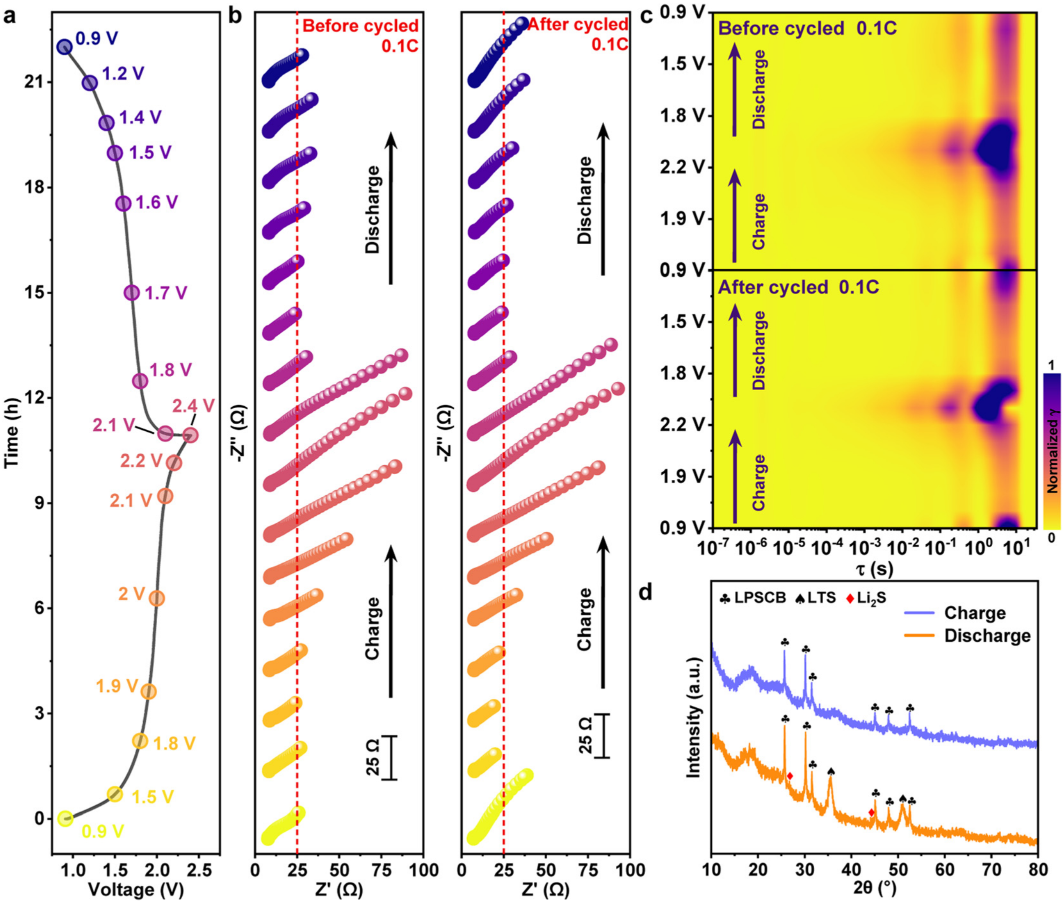

Fig. 4 Electrochemical evolution process of high-load LTS/LPSCB/Li–In batteries during operation. (a) Voltage–time curve of ASSLBs during cycling at 0.1C. (b) *In situ* EIS spectra of ASSLBs before cycling and after 20 cycles. (c) The corresponding 2D intensity mapping of DRT curves of the ASSLBs. (d) XRD patterns of the composite cathode at fully charged and fully discharged states.

certain electrochemical details, the overall trend of impedance evolution remains consistent with that observed during cycling at 0.1C.

Furthermore, XRD patterns of the cathode side in LTS/LPSCB/Li–In batteries under fully charged and fully discharged conditions are displayed in Fig. 4d. Analysis confirms that the sulfide–silver–germanium phase characteristic of the LPSCB electrolyte remains structurally stable across both extreme potentials, exhibiting no evidence of decomposition into secondary phases. Under the fully delithiated condition, diffraction peaks associated with LTS nearly disappear, indicating extensive Li extraction and structural transformation. In contrast, under the fully lithiated condition, the principal diffraction peaks of LTS are distinctly restored. Minor reflections located at 27.0° and 45.0° correspond to Li_2S, corroborating earlier findings regarding the generation of byproducts induced by over-lithiation.

Mechanical stress represents a pervasive factor governing the electrochemical behavior of lithium batteries during operation. In ASSLBs, external stack pressure, solid–solid interfacial contact, and intrinsic material expansion collectively modulate internal electrochemical and mechanical dynamics.[46,47] Further insight into electro–chemo–mechanical coupling within LTS/LPSCB/Li–In batteries was obtained through *in situ* pressure measurements employing a pressure sensor integrated into a standard battery configuration. Fig. 5a presents the synchronous evolution of internal pressure during charge–discharge cycling under conventional cathode loading. Internal stress progressively increases with rising charge potential, exhibiting a maximum growth rate of approximately 2.1%. During cathode lithiation, stress decreases in concert with discharge, and the rate of stress relaxation closely parallels the evolution of capacity. Such behavior indicates that internal expansion is predominantly driven by lithiation of the Li–In anode, whereas the LTS cathode contributes only minor, step-like perturbations superimposed on a nearly linear background due to its limited volumetric variation.

In situ pressure measurements under high cathode loading reveal a qualitatively similar but quantitatively amplified trend (Fig. 5b). Step-like perturbations become substantially diminished, accompanied by a pronounced increase in stress growth rate to approximately 3.6%. The enhanced stress response originates from the higher stacking rigidity of the densified

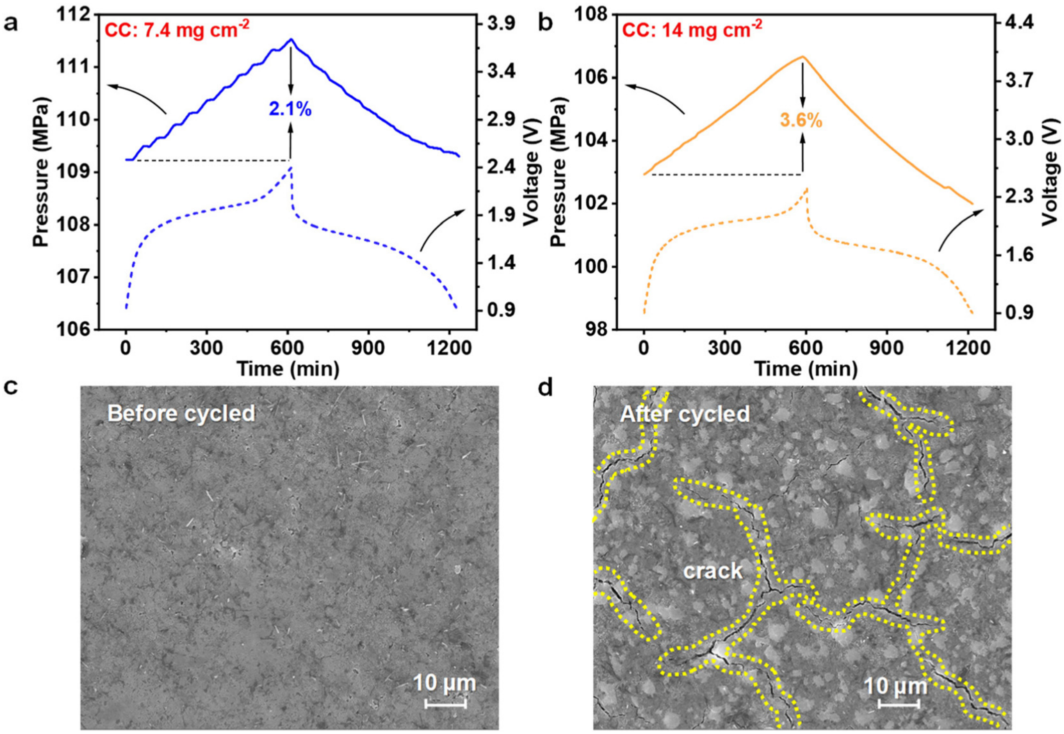

Fig. 5 Electromechanical coupling behavior in LTS/LPSCB/Li–In ASSLBs. (a) *In situ* pressure evolution alongside the corresponding charge–discharge voltage profiles for ASSLBs under conventional loading; (b) the same measurements for ASSLBs under high loading. Surface SEM image of an all-solid-state battery (c) before and (d) after cycling.

cathode layer, which constrains anode expansion and thereby amplifies the mechanical feedback for a comparable volumetric change. Evaluation of strain behavior after extended cycling under high loading was further conducted *via* SEM characterization of the cathode surface before and after cycling (Fig. 5c and d). The pristine electrode exhibits a smooth surface with compact particle contacts, whereas after 400 cycles, multiple extended cracks are observed. Nanoscale imaging confirms that LTS particles retain structural integrity (Fig. S8, shown in SI), implying that crack formation primarily arises from localized interfacial separation induced by stress inhomogeneity accumulated during long-term cycling. Considering the overall stress evolution, LTS demonstrates favorable stress adaptability during repeated lithiation–delithiation. Mitigation of mechanical degradation in such solid-state systems should therefore prioritize optimization of the anode configuration.

4. Conclusion

This work systematically investigates the evolution of surface morphology, crystal structure, and electrochemical properties of halogen-rich lithium argyrodites ($Li_{5.5}PS_{4.5}Cl_{0.8}Br_{0.7}$) synthesized *via* high-energy ball milling, with varying filling rate of milling balls (FRB) and ball-to-material ratios (BMR). Analysis of ball-milling parameters reveals that a 10% FRB combined with an 80 : 1 BMR optimizes ionic transport properties of LPSCB electrolytes, achieving a peak ionic conductivity of 13.3 mS cm^{-1} and an activation energy of 0.28 eV after sintering. Structural analysis confirms that ball-milling does not induce phase transformations, preserving the cubic argyrodite structure ($F\bar{4}3m$), while significantly influencing defect engineering and residual stress. Contrary to conventional understanding, increased BMR reduces unit cell volume while enhancing ionic conductivity, suggesting that ionic transport is governed not by lattice expansion, but by the interplay of energy input, defect density, and stress modulation. High BMR (80 : 1) effectively suppresses LiCl precipitation *via* enhanced amorphization, while insufficient milling energy (5% FRB) leaves residual Li_2S precursors, introducing deep-level defects that compromise long-term stability. The optimized electrolyte demonstrates stable performance (13–14 mS cm^{-1}) across varying mass loadings (100–200 mg), confirming its practical viability.

Li_2TiS_3 (LTS), a superionic conductor with excellent chemical compatibility with sulfide electrolytes, overcomes the oxidation stability limitations of LPSCB, enabling the development of high-performance ASSLBs. Under conventional loading (7.6 mg cm^{-2}), the LTS/LPSCB/Li–In battery exhibits outstanding reversible capacity (470.6 mAh g^{-1}) and excellent cycling stability (96.22% retention after 200 cycles), validating the system's effective suppression of electrolyte oxidative decomposition and promoting highly reversible Li^+ transport.

Under high loading (14 mg cm^{-2}), the battery achieves an initial capacity of 384.4 mAh g^{-1}, but cycle life is significantly shortened (67.2% retention after 400 cycles). Electrochemical impedance spectroscopy and relaxation time distribution analysis reveal a four-stage diffusion-controlled kinetic process: (1) activation phase (0.9–1.9 V), (2) de-lithiation phase (1.9–2.4 V), (3) lithiation phase (2.4–1.6 V), and (4) deep discharge stage (<1.6 V). *In situ* stress testing indicates that internal stress is generated by anode expansion and amplified by cathode constraint, while crack formation on the cathode surface reflects the accumulated mechanical fatigue during long-term cycling. Under high loading, stress growth increases to 3.6%, leading to cathode interface cracking after 400 cycles, confirming that mechanical–electrochemical coupling failure is critical for long-cycle performance degradation. This study establishes LTS as a viable high-performance cathode for sulfide-based all-solid-state batteries and emphasizes the need for interface engineering and anode stress management to balance energy density and cycle life.

Conflicts of interest

The authors declare no competing financial/commercial interests.

Data availability

All data included in this study are available upon request by contact with the corresponding author.

Acknowledgements

This work was supported by relevant National programmes of China. It was also supported by the National Key Research and Development Program (no. 2021YFB2500200). This work is also supported by the National Natural Science Foundation of China (no. 52177214) and Shanghai Automotive Industry Science and Technology Development Foundation. We gratefully acknowledge the Analytical and Testing Center of HUST, Instrumental Analysis Center of Xidian University and Comprehensive Experimental Center for Chemistry and Bioscience in Xidian University allow us to use the facilities.

References

1 R. F. Service, *Science*, 2019, **365**, 108.
2 X. Min, L. Wang, M. Shen, G. Ma and X. He, *Mater. Today*, 2025, **83**, 157–165.
3 V. Nguyen-Tien, C. Zhang, E. Strobl and R. J. R. Elliott, *Nat. Energy*, 2025, **10**, 354–364.
4 Y. Zhang, J. Sun, L. Li, Z. Long, P. Meng, E. H. Ang and Q. Liang, *Coord. Chem. Rev.*, 2025, **528**, 216432.
5 D. Li, Y. Li, H. Liu, M. Wu, X. Qi, C.-W. Nan and L.-Z. Fan, *Interdiscip. Mater.*, 2025, **4**, 775–785.
6 X. Gao, Y. Chen, Z. Zhen, L. Cui, L. Huang, X. Chen, J. Chen, X. Chen, D.-J. Lee and G. Wang, *Nano-Micro Lett.*, 2025, **17**, 140.
7 R. Ma, S. Pan, H. Wu, Y. Deng, Y. Wu, Y. Luo, Y. Lin, Q. Wang, P. Chen, Z. Gong and Y. Yang, *Chem. Rev.*, 2025, **125**, 10802–10875.
8 V. Siller, L. Xu, L. Castro, A. Gueguen and M. El Kazzi, *Small*, 2025, **21**, e08796.
9 S.-J. Tan, J. Yue, Z. Chen, X.-X. Feng, J. Zhang, Y.-X. Yin, L. Zhang, J.-C. Zheng, Y. Luo, S. Xin and Y.-G. Guo, *Energy Mater. Adv.*, 2024, **5**, 0076.
10 Z. Lu, S. Li, L. Ming, Z. Jiang, L. Li, Q. Luo, M. Deng, C. Liu and C. Yu, *J. Electroanal. Chem.*, 2026, **1000**, 119624.
11 L. Li, S. Liu, S. Li, Z. Jiang, Q. Luo, Z. Lu, M. Deng, W. Tian, J. Yang, C. Liu, Q. Wang and C. Yu, *Chem. Eng. J.*, 2025, **526**, 171209.
12 Q. Luo, L. Ming, D. Zhang, C. Wei, Z. Wu, Z. Jiang, C. Liu, S. Liu, K. Cao, L. Zhang, C. Yu and S. Cheng, *Energy Mater. Adv.*, 2023, **4**, 0065.
13 S. Chen, C. Yu, C. Wei, Z. Jiang, Z. Zhang, L. Peng, S. Cheng and J. Xie, *Energy Mater. Adv.*, 2023, **4**, 0019.
14 X. Zhao, L. Shen, N. Zhang, J. Yang, G. Liu, J. Wu and X. Yao, *Energy Mater. Adv.*, 2024, **5**, 0074.
15 L. Huang, L. Zhang, J. Bi, T. Liu, Y. Zhang, C. Liu, J. Cui, Y. Su, B. Wu and F. Wu, *Energy Mater. Adv.*, 2024, **5**, 0092.
16 S. H. Choi, W.-J. Kim, B.-h. Lee, S.-C. Kim, J. G. Kang and D.-W. Kim, *J. Mater. Chem. A*, 2023, **11**, 14690–14704.
17 M. Otoyama, A. Sakuda, M. Tatsumisago and A. Hayashi, *ACS Appl. Mater. Interfaces*, 2020, **12**, 29228–29234.
18 K. Kanazawa, S. Yubuchi, C. Hotehama, M. Otoyama, S. Shimono, H. Ishibashi, Y. Kubota, A. Sakuda, A. Hayashi and M. Tatsumisago, *Inorg. Chem.*, 2018, **57**, 9925–9930.
19 J.-F. Zhuo and Z.-F. Yao, *Solid State Ion.*, 2025, **423**, 116813.
20 S. Wang, A. Gautam, X. Wu, S. Li, X. Zhang, H. He, Y. Lin, Y. Shen and C.-W. Nan, *Adv. Energy Sustainability Res.*, 2024, **5**, 2200197.
21 P. Cao, J. Chen, J. Li, H. Yu, J. Lin, Z. Tian, G. Liu and X. Yao, *Small*, 2025, **21**, 2501901.
22 J. Liu, S. Wang, Y. Qie and Q. Sun, *Mater. Today Energy*, 2021, **21**, 100719.
23 C. Dong, Z. Bi, R. Li, Y. Ma, B. Li, H. Shi, Z. Zhang and Z.-S. Wu, *Natl. Sci. Rev.*, 2025, **12**, nwaf217.
24 Q. Luo, S. Li, L. Li, Z. Jiang, Z. Lu, W. Hu, M. Deng, J. Yang, Z. Wang, C. Liu and C. Yu, *Chem. Eng. J.*, 2025, **523**, 168270.
25 J.-U. Cho, R. Rajagopal, D. H. Yoon, Y. J. Park and K.-S. Ryu, *Chem. Eng. J.*, 2023, **452**, 138955.
26 Y. Hu, Z. Sun, Z. Zhang, S. Liu, F. He, Y. Liu, Z. Zhuang and F. Liu, *Adv. Energy Mater.*, 2023, **13**, 2202756.
27 L. Ming, L. Li, C. Wei, C. Liu, Z. Jiang, S. Li, Z. Wu, Q. Luo, Y. Wang, L. Zhang, X. Chen, S. Cheng and C. Yu, *Appl. Mater. Today*, 2024, **40**, 102410.
28 K. Sau, S. Takagi, T. Ikeshoji, K. Kisu, R. Sato, E. C. dos Santos, H. Li, R. Mohtadi and S.-i. Orimo, *Commun. Mater.*, 2024, **5**, 122.

29 T. Wu, S. Chen, Z. Su, Z. Wang, P. Luo, Z. Zheng, J. Luo, H. Ma, X. Zhang and G. Liang, *Nat. Energy*, 2025, **10**, 630–640.

30 A. Gautam, M. Ghidiu, A.-L. Hansen, S. Ohno and W. G. Zeier, *Inorg. Chem.*, 2021, **60**, 18975–18980.

31 S. Li, J. Lin, M. Schaller, S. Indris, X. Zhang, T. Brezesinski, C.-W. Nan, S. Wang and F. Strauss, *Angew. Chem., Int. Ed.*, 2023, **62**, e202314155.

32 P. M. G. Puente, S. Song, S. Cao, L. Z. Rannalter, Z. Pan, X. Xiang, Q. Shen and F. Chen, *J. Adv. Ceram.*, 2021, **10**, 933–972.

33 W. Sha and H. K. D. H. Bhadeshia, *Mater. Sci. Eng., A*, 1997, **223**, 91–98.

34 T. Sakai and J. J. Jonas, *Acta Metall.*, 1984, **32**, 189–209.

35 K. K. Alaneme and E. A. Okotete, *J. Sci.: Adv. Mater. Devices*, 2019, **4**, 19–33.

36 A. Sakuda, T. Takeuchi, K. Okamura, H. Kobayashi, H. Sakaebe, K. Tatsumi and Z. Ogumi, *Sci. Rep.*, 2014, **4**, 4883.

37 M. Fantauzzi, B. Elsener, D. Atzei, A. Rigoldi and A. Rossi, *RSC Adv.*, 2015, **5**, 75953–75963.

38 M. Liu, A. Song, X. Zhang, J. Wang, Y. Fan, G. Wang, H. Tian, Z. Ma and G. Shao, *Nano Energy*, 2025, **136**, 110749.

39 Y. Jung, Y.-Y. Song, Y.-S. Kim, Y. Chung, D.-H. Lee, S.-W. Park, H. Kim, H.-S. Min, J. Park, J. Seong, S.-K. Jung and D.-H. Seo, *EcoMat*, 2024, **6**, e12502.

40 S. Wang, M. Tang, Q. Zhang, B. Li, S. Ohno, F. Walther, R. Pan, X. Xu, C. Xin, W. Zhang, L. Li, Y. Shen, F. H. Richter, J. Janek and C.-W. Nan, *Adv. Energy Mater.*, 2021, **11**, 2101370.

41 W. Cun, Z. Wei-jiang, H. Teng-fei, L. Bo, S. You-jie, Z. Yao-dong, L. Wei-lin and J. Fang-ming, *J. Electrochem.*, 2020, **26**, 777.

42 D. H. S. Tan, E. A. Wu, N. Han, Z. Chen, M. A. T. Marple, J.-M. Doux, X. Wang, H. Yang, A. Banerjee and Y. S. Meng, *ACS Energy Lett.*, 2019, **4**, 2418–2427.

43 Z. Lu, S. Li, L. Li, L. Ming, Z. Jiang, M. Deng, Z. Wang, C. Liu and C. Yu, *J. Mater. Chem. A*, 2025, **13**, 20477–20487.

44 K. Kobayashi and T. S. Suzuki, *Electrochemistry*, 2022, **90**, 017004.

45 Y. Hase, T. Uyama, K. Nishioka, J. Seki, K. Morimoto, N. Ogihara, Y. Mukouyama and S. Nakanishi, *J. Am. Chem. Soc.*, 2022, **144**, 1296–1305.

46 J. Gu, X. Chen, Z. He, Z. Liang, Y. Lin, J. Shi and Y. Yang, *Adv. Energy Mater.*, 2023, **13**, 2302643.

47 J. Gu, X. Chen, Z. Liang, H. Zhong, J. Shi and Y. Yang, *Energy Storage Mater.*, 2023, **63**, 103052.